Crystal and electronic facet analysis of ultrafine Ni_2P particles by solid-state NMR nanocrystallography

Wassilios Papawassiliou[1], José P. Carvalho[1], Nikolaos Panopoulos[2], Yasser Alwahedi[3]*, Vijay Kumar Shankarayya Wadi[3], Xinnan Lu[3], Kyriaki Polychronopoulou[3], Jin Bae Lee [4], Sanggil Lee [4], Chang Yeon Kim[4], Hae Jin Kim[4], Marios Katsiotis[3], Vasileios Tzitzios[2], Marina Karagianni[2], Michael Fardis[2], Georgios Papavassiliou[2]* and Andrew J. Pell[1,5]*.

[1] Department of Materials and Environmental Chemistry, Arrhenius Laboratory, Stockholm University, Svante Arrhenius väg 16 C, SE-106 91 Stockholm, Sweden,

[2] Institute of Nanoscience and Nanotechnology, National Center for Scientific Research "Demokritos", 153 10 Aghia Paraskevi, Attiki, Greece,

[3] Department of Chemical Engineering, Khalifa University, PO Box 2533, Abu Dhabi, United Arab Emirates,

[4] Electron Microscopy Research Center, Korea Basic Science Institute, 169-148 Gwahak-ro, Yuseong-gu, Daejeon 34133, Republic of Korea,

[5] Centre de RMN à Très Hauts Champs de Lyon (FRE 2034 - CNRS, ENS Lyon, UCB Lyon 1), Université de Lyon, 5 rue de la Doua, 69100 Villeurbanne, France.

*yasser.alwahedi@ku.ac.ae, g.papavassiliou@inn.demokritos.gr, andrew.pell@mmk.su.se

Abstract: Structural and morphological control of crystalline nanoparticles is crucial in the field of heterogeneous catalysis and the development of "reaction specific" catalysts. To achieve this, colloidal chemistry methods are combined with ab initio calculations in order to define the reaction parameters, which drive chemical reactions to the desired crystal nucleation and growth path. Key in this procedure is the experimental verification of the predicted crystal facet and its corresponding electronic structure, which in case of nanostructured materials becomes extremely difficult. Here, by employing ^{31}P solid-state nuclear magnetic resonance (ssNMR) aided by advanced density functional theory (DFT) calculations to obtain and assign the Knight shifts, we succeeded in determining the crystal and electronic structure of the terminating surfaces of ultrafine Ni_2P nanoparticles at atomic scale resolution. Our work highlights the potential of ssNMR nanocrystallography as a unique tool in the emerging field of facet-engineered nanocatalysts.

Introduction

Shape and size engineering of functional nanocrystalline materials is an area of major scientific and technological interest[1-3]. This is because in many important applications which rely on surface structure and chemistry, such as heterogeneous catalysis, gas sensing, and energy conversion and storage, the properties of the materials can be tailored by controlling the size, crystal structure, and morphology of the external surfaces of the constituent particles[4-6]. For heterogeneous catalysis, scaling down the particle size not only increases the number of catalytic sites, but also modifies the electronic properties. Furthermore, the catalytic reactivity and selectivity changes by modifying the arrangement and coordination of the surface atoms, thus becoming very sensitive to the enclosing crystal facets. In this context a lot of effort has been devoted in order to understand the role of the facet morphology and crystal structure on the catalytic reactivity of Ni_2P nanoparticles, a staple in the area of research of many important catalytic processes, such as the electrocatalytic hydrogen evolution reaction (HER)[7] and oxygen evolution reaction (OER)[8], the water-gas shift reaction[9], as well as the hydrodeoxygenation and the hydrodesulfurization (HDS) of hydrocarbons[10].

Ni_2P adopts an ABAB two-layer arrangement along the (0001) direction of the crystal structure, as shown in Figure 1d, in which the alternating layers have stoichiometries Ni_3P and Ni_3P_2, and which compete for the possession of the 0001 surface. First principles calculations[11] have shown that Ni_3P_2 termination is energetically favored in comparison to Ni_3P termination, while experiments indicate that the hexagonal 0001 surface is terminated primarily by P-covered Ni_3P_2 (Ni_3P-P)[12,13], where P adatoms stabilize the surface with the dangling bonds of threefold Ni atoms. These exposed 0001 facets have shown higher efficiency in the catalytic activity of Ni_2P nanoparticles[14]. However, the stability of differently terminated Ni_2P surfaces depends on the experimental synthesis conditions, and these effects are not yet sufficiently well understood. For instance, atomistic thermodynamic studies of the stability of different low-Miller-index Ni_2P surfaces, by considering different temperatures, pressures, and chemical potentials, have shown that the equilibrium morphology of the Ni_2P nanoparticles comprises mainly 0001, $10\bar{1}0$ and $101\bar{1}$ facets; similarly, Ni_2P nanowires expose 0001, and $10\bar{1}0$ surfaces[15].

As solid-state nuclear magnetic resonance (ssNMR) is sensitive to the structure and electronic environment at the atomic (local) scale, it is able to determine the distinct surface facets in nanosized particles as well as distinguish between these and the bulk-like interior of the nanoparticle[16-19]. In the case of nanocrystalline metallic powders, the strength of ssNMR lies in its ability to probe the interactions which couple the conduction electrons with the nuclear

spins, via the Knight shift[20] $K = K_{FC} + K_{dip} + K_{orb}$. Here, K_{orb} is the orbital part of the Knight shift, induced by the response of the orbital motions of all electrons to the applied external magnetic field, and K_{FC} and K_{dip} are the Fermi-contact and spin-dipolar parts of the Knight shift, respectively, due to the contact and dipolar parts of the hyperfine interaction of the nuclear spins with the net electron magnetic moment of the conduction electrons, again induced by the external magnetic field[21, 22].

In metallic systems, to a first non-interacting electrons approximation, K_{FC} is approximated by:

$$K_{FC} = \frac{8\pi}{3} \left\langle |\varphi_s(0)|^2 \right\rangle_F \mu_B{}^2 N(E_F) \qquad (1),$$

where $\langle|\varphi_s(0)|^2\rangle$ is the probability density of the s–band electrons within the nuclear volume evaluated near the Fermi level, $N(E_F)$ is the s electron projected density of states (pDOS) at the Fermi level, and μ_B is the Bohr magneton. This Fermi-contact term is often the dominant contribution to the Knight shift in metallic materials[21,23,24,25,] and equips NMR with the opportunity to experimentally probe the local electronic density of states near the Fermi level, with obvious significance for chemistry and catalysis, as the ratio between the density of localized and delocalized electrons near the Fermi level induces greatly affects the catalytic properties[26].

In this context, we have employed density-functional-theory (DFT)-assisted ^{31}P ssNMR combined with experimental and theoretical X-ray diffraction (XRD) and transmission electron microscopy (TEM) (i.e. experimental and DFT-calculated XRD and TEM) to (i) identify the dominant crystal facets of ultrafine Ni_2P nanoparticles and (ii) visualize the subtle structural and electronic changes that take place on these surfaces, with respect to the bulk interior of the nanoparticles. Results show that the Ni_3P_2–terminated surfaces, from now on labeled as 0001-A crystal facets, prevail over the Ni_3P-terminated surfaces, 0001-B, where the phosphorus atoms are placed at a different Wyckoff position, while Ni(1) and Ni(2) atoms within a few surface layers acquire similar crystal symmetry and electron DOS. Most importantly, the nanoparticles appear to have a thin rod-like shape with lateral $10\bar{1}0$ surfaces that become more prevalent by increasing size of the nanoparticles. At the same time, on both terminating surfaces, the Ni d-electron bands shift towards the Fermi level, verifying that the highly enhanced catalytic activity of the Ni_2P nanoparticles to a great extent originates from the changes in the surface electronic properties.

This is the first time that facet analysis of a transition metal nanocatalyst and the relevant electronic changes are experimentally revealed, showcasing that ssNMR nanocrystallography is an unparalleled tool in the study of metallic nanocatalysts.

Results

^{31}P ssNMR and DFT calculations of microcrystalline (bulk) Ni_2P

The potential of DFT-assisted ssNMR to acquire accurate structural and electronic information on transition metal phosphides is showcased in Figure 1. Microcrystalline Ni_2P is known to adopt the hexagonal structure assigned to the Fe_2P structure type, with space group *P*-62*m*[28]. This structure can be visualized as an alternation of two nonequivalent atomic layers along the 0001 direction with stoichiometry of Ni_3P_2 and Ni_3P. Nickel and phosphorous atoms in the two layers are labeled as Ni(1)/P(1) (A-layer) and Ni(2)/P(2) (B-layer), respectively (Figure 1d). Figure 1a presents the ^{31}P magic-angle-spinning (MAS) ssNMR spectrum of microcrystalline Ni_2P, and comprises two primary resonances: one with an isotropic shift at 4072 ppm, which is attributed to the P(1) site, and the second at 1468 ppm, attributed to P(2), in agreement with previous studies[27]. In addition, two weak NMR resonances accompanied by their respective spinning-sideband (SSB) manifolds are observed between 1800-2250 ppm and are attributed to the two non-equivalent P sites of a minority $Ni_{12}P_5$ phase. To confirm this assignment, the NMR shifts and shift anisotropies were calculated by DFT, using the Ni_2P atomic positions determined from the Rietveld analysis of the XRD pattern (Supplementary Figure 1a). The resulting simulated ^{31}P NMR spectrum (Figure 1b) shows an excellent match with the experimental ^{31}P NMR data.

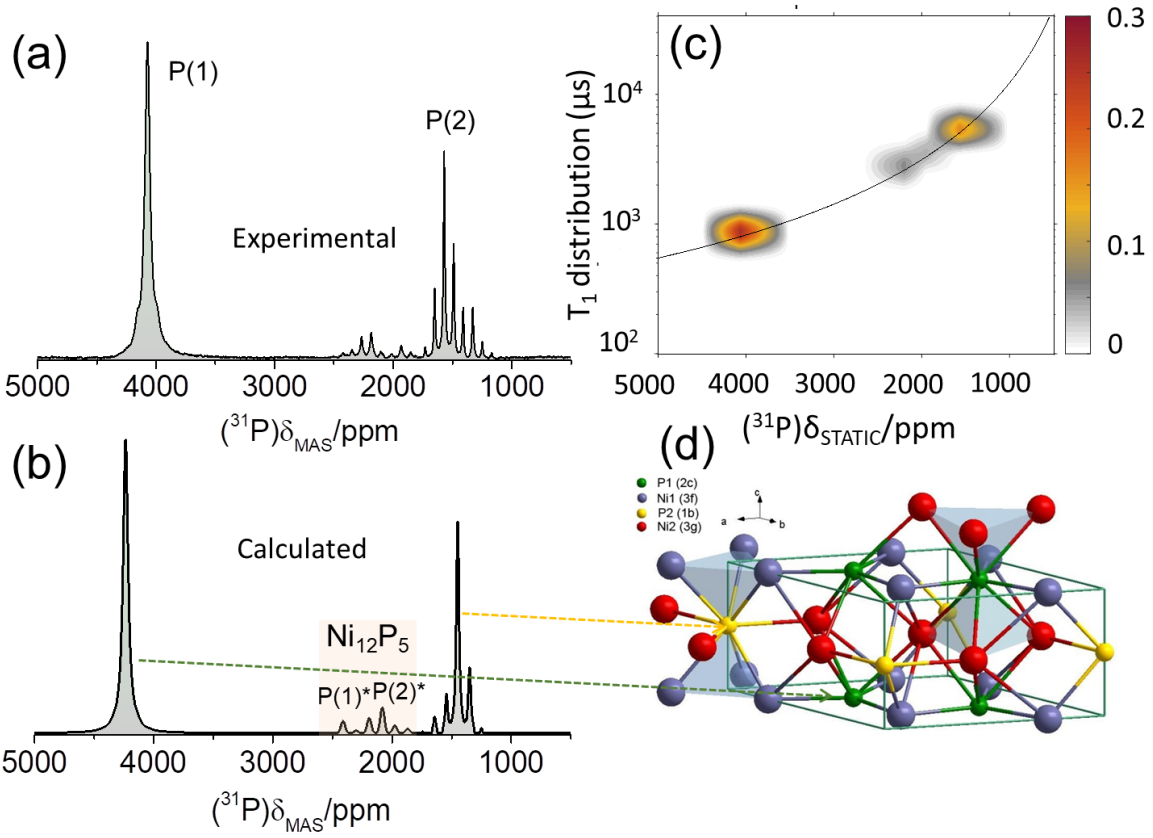

Fig. 1. ^{31}P ssNMR, spin-lattice relaxation analysis and DFT-calculated spectra of microcrystalline Ni_2P. **a.** ^{31}P NMR spectrum of microcrystalline Ni_2P at 14 kHz MAS. **b.** Simulated ^{31}P MAS NMR spectrum with the DFT-calculated Knight shifts. **c.** Spin-lattice relaxation times T_1 vs. NMR shift for microcrystalline Ni_2P under static conditions. The superimposed curve is fitted according to the Korringa relation (Equation S3 in Supplementary Note 5). **d.** Visualization of the crystallographic unit cell and its non-equivalent Ni and P sites.

The significant difference between the Ni-P bond lengths (5.85 Å for Ni(2)-P(2) and 3.38 Å for Ni(1)-P(1)), is crucial in the electronic structure of Ni_2P as it leads to higher DOS of the s orbitals of the P(1) atoms at the Fermi level $N(E_F($ Supplementary Figures 5c,d, thus causing the significantly higher Knight shift K_{tot}. Specifically, the ratio of pDOS(P(1))/pDOS(P(2)) ≈ 2.67 for the s-electrons is approximately equal to the ratio of experimental Knight shifts K(P(1))/K(P(2)) ≈2.8, indicating that conduction electrons, especially of P(1) atoms, are in excess on the Ni_3P_2 A-layer in comparison to the P(2) atoms on the Ni_3P B-layer, as observed in Supplementary Figures 5c,d. Furthermore, the pDOS values are in accordance with the calculated total (isotropic) ^{31}P NMR Knight shift, referenced according to the relation $K=\sigma_{ref} - \sigma_{calc}$. In this formula σ_{ref}=220.23 ppm is the reference ^{31}P NMR shielding, calculated with the procedure used by Mayo et al.[29] (see Supplementary Figure 10), and σ_{calc} is the total DFT

calculated ^{31}P NMR shielding in Ni_2P, which is equal to $\sigma_{calc} = \sigma_{FC} + \sigma_{dip} + \sigma_{orb}$[16]. According to the DFT calculations, the Fermi-Contact shielding σ_{FC} is the primary contribution responsible for the large NMR shift difference between the two non-equivalent sites (σ_{FC} is equal to -4085 ppm for P(1) and -1061ppm for P(2)), while the orbital contribution is smaller (σ_{orb} = 70.72 ppm for P(1) and -150.29 for P(2)), and the dipolar term σ_{dip} is negligible (of the order of a few ppm for both P(1) and P(2)). At the same time, the P(2) atoms on the Ni_3P layer probe an increased orbital current anisotropy, as manifested by the broader SSB manifold of this resonance. In addition, the ^{31}P NMR signals from the minority $Ni_{12}P_5$[30] phase were reproduced by DFT calculations in a similar manner. Our ^{31}P NMR Knight shift analysis is in full accordance with the spin–lattice relaxation time T_1 measurements performed in the temperature range 290 K to 500 K, which are presented in Figure 1c and Supplementary Figure 14; these data demonstrate excellently the metallic character of Ni_2P, since the Knight shifts and relaxation times together follow the Korringa relation[25], described in Supplementary Note 5. Specifically, $T_1(P(2))/T_1(P(1)) \approx (K(P(1))/K(P(2)))^2 \approx 7.85$, in agreement with the Korringa relation in equation (S3) .

Scaling down to nano-sized particles

On the basis of the above results the question that arises, is whether ssNMR is able to monitor the evolution of the crystal and electronic structure of Ni_2P, when the system dimensions shrink from a microcrystalline to a nano-crystalline structure, as this scaling down is predicted to expose a greater particle surface area, and a variety of crystal facets.[15] In general, the ability of XRD for accurately and precisely determining the crystal structure of the Ni_2P nanoparticles is greatly retarded on reducing the particle size, because the XRD peaks are broaden and merge, according to the Scherrer relation, as described in Supplementary Figure 1b. Fortunately, ssNMR still provides important structural data, again in the form of Knight shifts, which are sensitive to the subtle structural and electronic changes induced by reducing the particle size, as demonstrated by the ^{31}P NMR spectra in Figure 2. Details on the synthesis and characterization of the examined Ni_2P nanoparticles are provided in the Materials and Methods section and the Supplementary Information. The presence of a $Ni_{12}P_5$ impurity phase that may occur as a byproduct during the synthesis of the nanoparticles is excluded, as explicitly shown by comparing the XRD patterns of the Ni_2P nanoparticles with the relevant XRD pattern of $Ni_{12}P_5$ nanoparticles, explicitly synthesized for this purpose (Supplementary Figures 1b and 3). While the NMR spectrum of Ni_2P nanoparticles with mean size of $d \approx 40$ nm , as determined from TEM, is similar to that of microcrystalline Ni_2P (upper panel in Figure 2a), upon reduction

of the nanoparticle size to 12 nm, the NMR signals broaden, and an extended spectral feature appears between the P(1) and P(2) resonances. This feature grows at the expense of the P(1) resonance, which has an integral that is reduced in comparison to P(2), similarly to observations previously reported for ZnSe nanoparticles[31]. Notably, there is no information gain with MAS spinning, at least for a spinning frequency for 14 kHz, as seen in the mid panel of Figure 2a. By further reducing the particle size the NMR signal becomes even broader extending in the spectral range between 0-5000 ppm, whilst most of the signal intensity of the P(1) resonance is shifted to lower shifts (lower panel of Figure 2a).

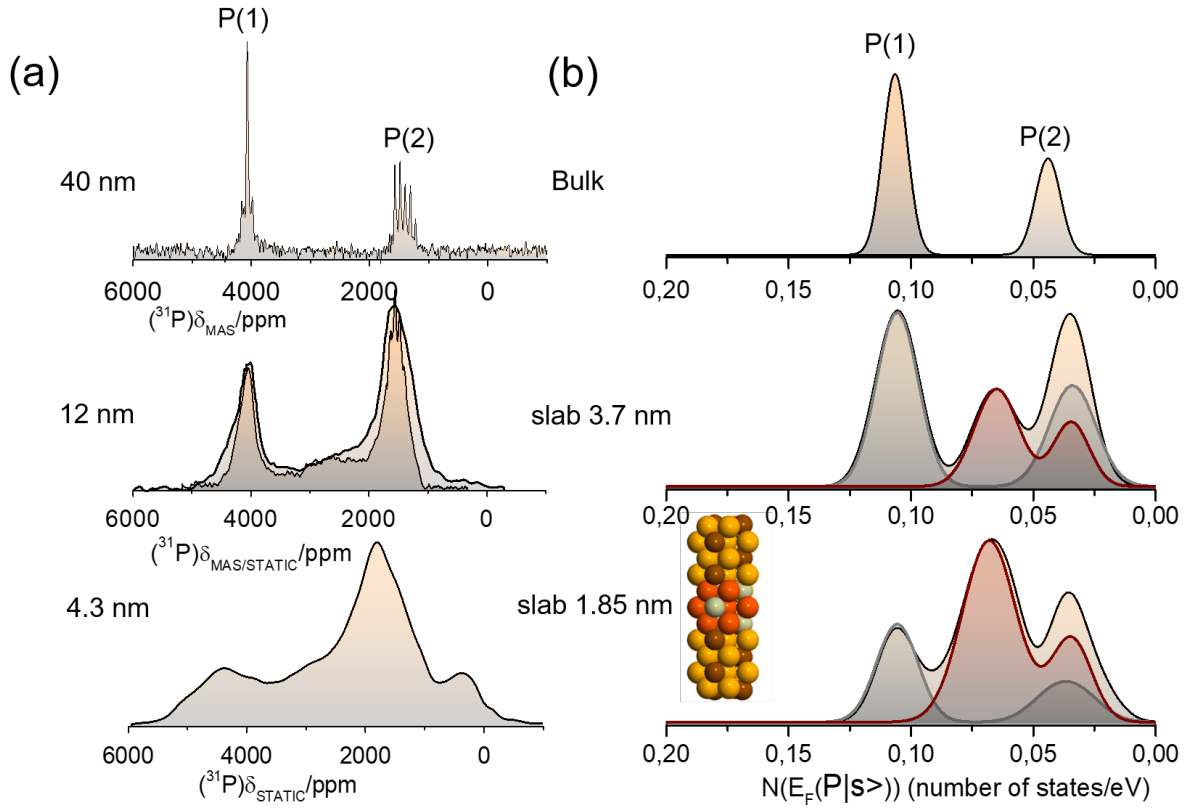

Fig. 2. Correlating ^{31}P ssNMR spectra with DFT calculations. **a.** From top to bottom: ^{31}P MAS at 14 kHz MAS and static NMR spectra of nanocrystalline Ni_2P with mean diameters d≈40 nm, 12 nm, and 4.3 nm. In the mid panel the overlaid spectrum is the relevant MAS spectrum. **b.** From top to bottom: Visualization of the phosphorous s-electrons pDOS distribution at the Fermi level $N(E_F(|s>))$, in bulk Ni_2P and two slabs with thickness 3.7 nm and 1.85 nm, respectively, with Ni_3P_2 terminating layers (0001-A). Lines in red and grey colors are the relevant pDOS contributions from surface and core-bulk-like phosphorous atoms, respectively. The bottom right insert displays the 0001-A super-cell with 50 atoms (1.85 nm),

with the orange and brown spheres representing the surface nickel and phosphorus atoms, while red and grey spheres represent the bulk nickel and phosphorus atoms respectively.

To correlate the changes in the NMR lineshapes with alterations in the surface electron states, DFT calculations of the electron DOS were performed on a number of Ni_2P slabs with different exposed surfaces. DOS plots of the two most common exposed surfaces, the 0001-A (with terminating Ni_3P_2 surfaces), and $10\bar{1}0$ are presented in the Supplementary Figures 7-9. Figure 2b displays the distribution of the projected DOS (pDOS) of the s electron states at the Fermi level $N(E_F(|s>))$ for all non-equivalent phosphorous atoms in three atomic arrangements: two 0001-A terminating slabs with thickness 1.85 nm (super-cell of 50 atoms) and 3.71 nm (super-cell of 104 atoms), respectively, and periodic Ni_2P. A remarkable correlation of the pDOS plots with the NMR lineshapes is revealed, especially in case of ultra-small nanoparticles, which follows the correlation between Knight shift and pDOS in equation (1). In particular, in the case of bulk Ni_2P two peaks are observed at pDOS values 0.108 states/eV and 0.043 states/eV, which are attributed to the P(1) and P(2) atomic sites, respectively. Notably, in the case of the two slabs, the pDOS of the P(1) surface states (red lines) appears to shift towards the P(2) DOS peak. Furthermore, by increasing the slab thickness the central "bulk"-like states (grey lines) gain in intensity, resembling the changes of the ^{31}P NMR lineshapes with increasing size in Figure 2a. Supplementary Figures 6 and 7 show clearly that the strong shift of the s-electrons pDOS of surface P(1) atoms is associated with substantial structural and electronic changes in the vicinity of the 0001-A terminating surface: whilst the central atoms keep the same Wyckoff symmetry positions in the P-62m[28] space group (Ni(1)(3f), Ni(2)(3g), P(1)(2c), P(2)(1b)), the symmetry of both Ni atoms at the surface coalesces to Ni(6i), while the symmetry of the two phosphorus atoms changes to P(1)(4h) and P(2)(2e). These crystal symmetry changes are reflected in the projected DOS of the surface atoms. Both Ni(1) and Ni(2) in the middle of the slab exhibit almost the same p-DOS as bulk Ni_2P, while surface Ni(1) atoms show a remarkable shift of their pDOS towards the Fermi level, acquiring a similar pDOS profile to the Ni(2) surface atoms. Accordingly, the pDOS of surface P(1) atoms is seen to shift towards the Fermi level.

Another widely-discussed terminating surface is the $10\bar{1}0$ surface. Figure 3a displays the phosphorous s-electrons pDOS distribution at the Fermi level $N(E_F(|s>))$ of a $10\bar{1}0$ facet slab comprising a super-cell of 54 atoms. Similarly to the 0001-A termination, the pDOS of the surface P(1) atoms shifts towards that of P(2), resulting in the formation of a characteristic

doubly-peaked distribution with a strong peak close to the position of P(2). Notably, in both the 0001-A and $10\bar{1}0$ studied cases, the pDOS of the surface d-electrons shifts towards the relevant Ni(2) pDOS, while at the slab center the bulk Ni_2P pDOS is retained (Supplementary Figures 8, 9).

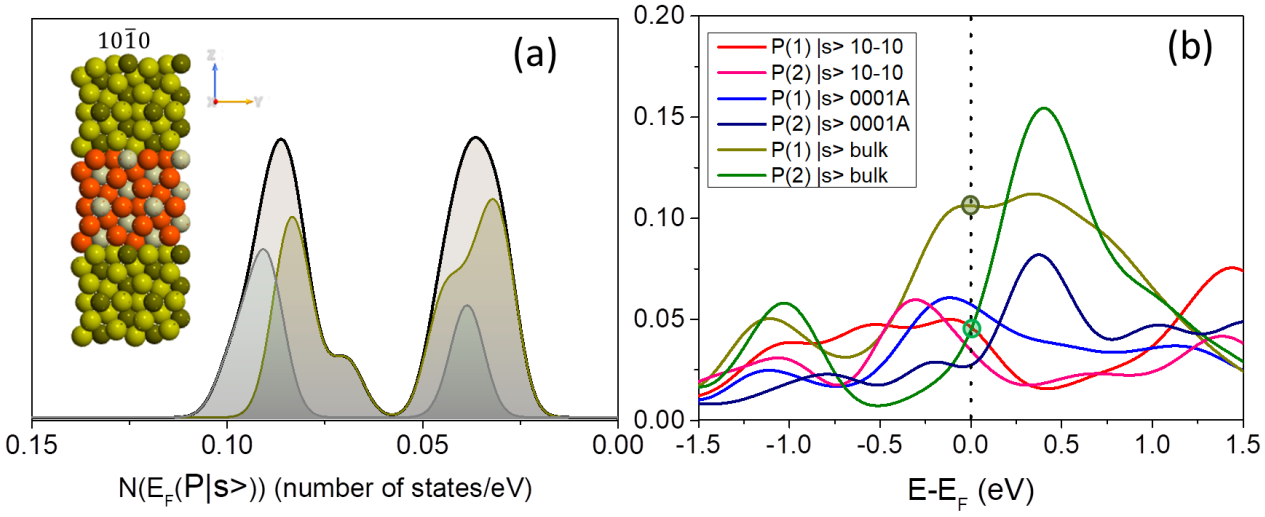

Fig 3. (a) The phosphorous s-electrons pDOS distribution at the Fermi level $N(E_F(|s>))$ of the $10\bar{1}0$ terminating slab. The inset shows the relevant 54-atoms super-cell, where the dark green and light green spheres represent the surface phosphorus and nickel respectively, while the red and grey spheres represent the bulk Ni and P. (b) The s-electrons pDOS of the P(1) and P(2) atomic positions in three different configurations: the 0001A, $10\bar{1}0$, and bulk Ni_2P. Circles indicate the pDOS values for bulk P(1) and P(2) atoms.

Figure 3b compares the s-electron pDOS of the outermost (surface) P(1) and P(2) atoms for the 0001-A, and $10\bar{1}0$ slabs, with that of the bulk Ni_2P. For reference, dark and light green circles indicate the pDOS at the Fermi level for bulk Ni_2P. In the case of the 0001-A facet, the pDOS of the P(1) edge atoms is shown to be significantly lower (0.0573 states/eV) than the pDOS of the central (bulk) atoms (0.108 states/eV), approaching that of the P(2) bulk atoms (0.0424 states/eV). Similarly, the P(2) edge atoms acquire a much lower pDOS (0.0275 states/eV) than the bulk-like central atoms. On the other hand, in the case of the $10\bar{1}0$ structure, the pDOS at the Fermi level of the edge P(1) and P(2) atoms, acquire similar values ~0.34 states/eV, that are close to that of bulk P(2). Hence, in the case that the 0001-A facet dominates the termination of the nanoparticles, NMR shift distribution is expected to appear between the P(1) and P(2) NMR peaks of the bulk material, due to the intermediate pDOS values, whereas

if the $10\bar{1}0$ facet prevails, the signal intensity is expected to increase at the shift of the P(2) NMR peak. Importantly, all structural and electronic changes are observed to take place within a few unit cells from the surface (see supplementary figures 6 and 7), thus showing that relatively "thin" slabs provide reliable calculated surface electronic properties, without any interference between atoms at the fringes of the two terminating surfaces.

Crystal facet determination of ultrasmall Ni_2P nanoparticles

In the previous section it was demonstrated that downsizing of the Ni_2P nanoparticles significantly modifies the electronic properties of the terminating surfaces. Although the exposure of specific facets is a crucial factor in optimizing the catalytic activity of the Ni_2P nanoparticles, this information is not readily accessible from XRD, whilst TEM and related techniques on the one hand provide exact structural information, but they barely provide any direct information on the electron band structure. By contrast, the Knight shift reflects both the structural *and* electronic changes that take place at the terminating surfaces. In order to determine the kind of exposed facets and the way that the electronic properties vary from the surface to the core of the Ni_2P nanoparticles, ^{31}P DFT- calculated NMR shifts were acquired, within the formalism of the WIEN2K code[32]. Four distinct facets were investigated: the 0001-A (Ni_3P_2 terminated), 0001-B (Ni_3P terminated), the 0001-A-P with extra P adatoms on top of the 0001-A surface, and the $10\bar{1}0$ facet. Wulff construction calculations[15] and a distinct number of experiments[33] indicate that nanoparticles and nanorods are eventually formed in the shape shown in Figure 4f. In this context, the calculated surfaces of the four distinct atomic configurations are depicted in Figure 4a-d, along with the DFT-calculated ^{31}P ssNMR spectra. Orange and green shaded areas in the calculated spectra are the ^{31}P NMR spectra of the 0001-A and $10\bar{1}0$ surface P-atoms respectively, and blue shaded areas are the calculated spectra from the central P-atoms with bulk-like character; the latter are shown in gray color in the insets of Figures 2b and 3a. In a similar manner to the bulk Ni_2P, the ^{31}P calculated Fermi contact shielding σ_{FC} is the dominates the orbital shielding (σ_{orb} takes values between -200 ppm to 200 ppm), while σ_{dip} is negligibly small. In case of the 0001-A terminating slab, the surface P(1) sites exhibit intense NMR peaks with shifts occupying the range 2000-3000 ppm (Figure 4a), resembling the relevant s-electrons pDOS in Figure 2b. In case of the 0001-B facets (Figure 4b) the P(1) surface sites exhibit peaks that are shifted from the bulk peak to a smaller extent than for the 0001-A facets.

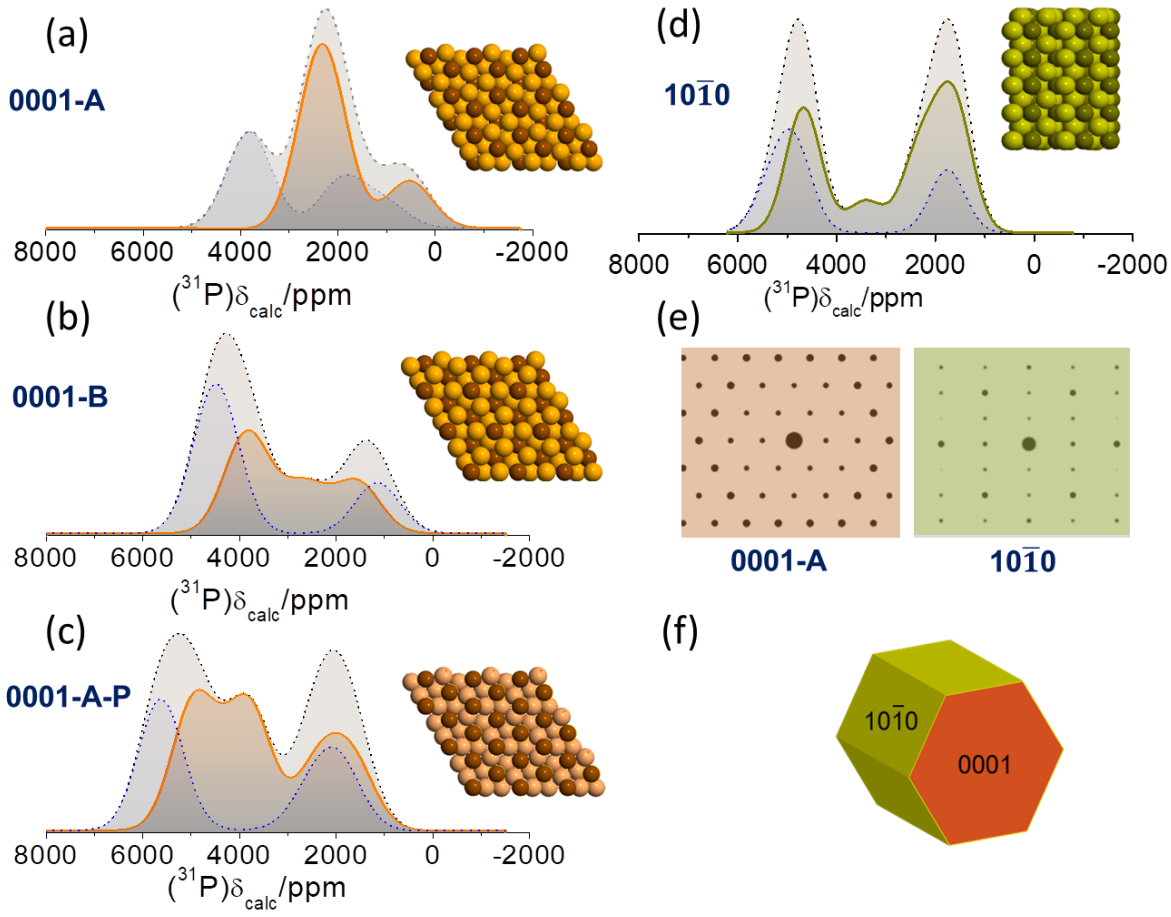

Fig 4. DFT calculated ^{31}P ssNMR spectra of 4 slabs with different terminating surfaces simulating facets of ultrasmall Ni_2P nanoparticles. NMR spectra from surfaces are in orange/green color, blue color spectral contribution is from the bulk-like interior. The total NMR spectrum is shown in yellow colour. **a.** ^{31}P DFT calculated NMR spectrum of a Ni_2P slab with 0001-A termination (super-cell with 50 atoms). **b.** ^{31}P DFT NMR spectrum of Ni_2P with 0001-B termination (49 atoms) **c.** ^{31}P DFT NMR spectrum of Ni_2P with $(0001-A-P)$ termination (52 atoms). **d.** ^{31}P DFT NMR spectrum of Ni_2P with $(10\bar{1}0)$ termination (54 atoms). **e.** The DFT calculated electron diffraction patterns (EDP) of the 0001-A and $10\bar{1}0$ terminating slabs, which are the two most common facets in the Ni_2P nanoparticles. **f.** Schematic presentation of a Ni_2P nanoparticle with 0001 (red) and the $10\bar{1}0$ (green) facets termination.

In the case of the 0001-A-P facet (Figure 4c) a positive frequency shift was observed for all P-atoms. This can be attributed to the reduction of the Ni atoms on the layers from Ni^{2+}/Ni^{3+} and Ni^{+}/Ni^{2+} in order to bond with the P-adatom, leading to more unpaired electrons that are delocalizing to the s-orbitals in the vicinity of the P atoms[34]. Finally, in case of the $10\bar{1}0$ terminating surface (Figures 4d), the calculated NMR spectrum consists of two well resolved primary peaks flanking a low intensity resonance, in agreement with the relevant pDOS of the

s-electrons $N(E_F(|s>))$ presented in Figure 3a, again demonstrating the prevalence of the Fermi contact term.

Figure 5 encapsulates the capacity of DFT-assisted ^{31}P NMR to acquire atomic-scale information on the crystal morphology and electronic structure of the surface of ultrafine Ni_2P nanoparticles with a mean size of 4.3 nm. The high-resolution TEM images shown in Figure 5a with the relevant electron diffraction patterns (EDPs) indicate the formation of hexagonally crystalized nanoparticles; however, it is difficult to make a full facet assignement with TEM. Comparison of the DFT calculated EDP of the $10\bar{1}0$ and 0001-A facets in Figure 4e with the experimental EDPs in Figure 5a unveils clearly the presence of nanoparticles exhibiting the $10\bar{1}0$ facet (further details are provided in Supplementary Figure 4), however, it is extermely difficult to acquire TEM images exhibiting the 0001-A facet. Until now, the formation of terminating 0001-A facets has been observed only by scanning tunneling microscopy maps of the Phosphorous atoms[12,13]. Furthermore, XRD, which in principle is able to resolve pristine 0001-A facets, does not lead to any definite conclusion, because the contribution of the 0001-A facets in the XRD pattern is masked by diffraction on both kinds of facets in combination with the Scherrer broadening, as clearly seen in Figure 5b. By contrast, DFT calculated ^{31}P ssNMR spectra (Figure 5c), , showcase unambiguosly the presence of both the 0001-A and $10\bar{1}0$ terminating surfaces. The experimental ^{31}P NMR spectrum exhibits a broad resonance at 2300 ppm and two "shoulders" at 4000 ppm and 500 ppm, accompanied by an additional feature at around 3000 ppm. The calculated NMR spectrum (overlaid on the experimental spectrum) was optimized by fitting (i) the intensity ratio of the NMR signals of the 0001-A and $10\bar{1}0$ facets, and (ii) the variance of the Gaussian function describing the lineshape (the NMR peaks were simulated by convoluting the calculated frequencies with a Gaussian function). At the same time the relevant calculated XRD pattern (red line overlaid on the experimental XRD pattern) was checked, in respect to the ratio of the two facet components, to ensure consistency with the experimental XRD pattern. It was found that the calculated NMR spectrum and XRD pattern are both in agreement with the experimental data only by combining the 0001-A with the $10\bar{1}0$ terminating surfaces in a ratio of ~1.77:1. This means that the Ni_2P nanoparticles have the morphology in the inset of Figure 5c[15]. Here we note that the calculation of the XRD patterns was benchmarked on microcrystalline Ni_2P also matches well with the experimental XRD pattern (shown in Supplementary Figure 1b). However, standalone fitting of the XRD pattern of the nanoparticles, without the use of NMR, is inconclusive with respect to the kind of facets enclosing the nanoparticle, due to the broader diffraction peaks.

The dominance of the surface effects in the 4.3 nm Ni_2P nanoparticles is furthermore evidenced by the $1/T_1T$ vs. T plots (where T is temperature) in Figure 5d. First of all, these measurements show that the Korringa relation, and thus the metallic character of the nanoparticles, is preserved. Besides, the enhancement of the $1/T_1T$ ratio on the two main NMR peaks of the nanosized system at frequencies 4380 ppm and 1776 ppm compared to the microcrystalline material (Supplementary Figure 14) implies that the s-electrons pDOS $N(E_F(|s>))$ at the Fermi level is increased, following Equation S3 in Supplementary Note 5. Overall, our NMR experiments validate the DOS plots presented in Supplementary Figures 7-10, and subsequently the shift of the Ni(1) d-electron DOS towards the Fermi level. This is important as, according to the d-band model of the catalytic activity,[26] it indicates the electronic origin of the enhanced catalytic activity of the Ni_2P nanoparticles.

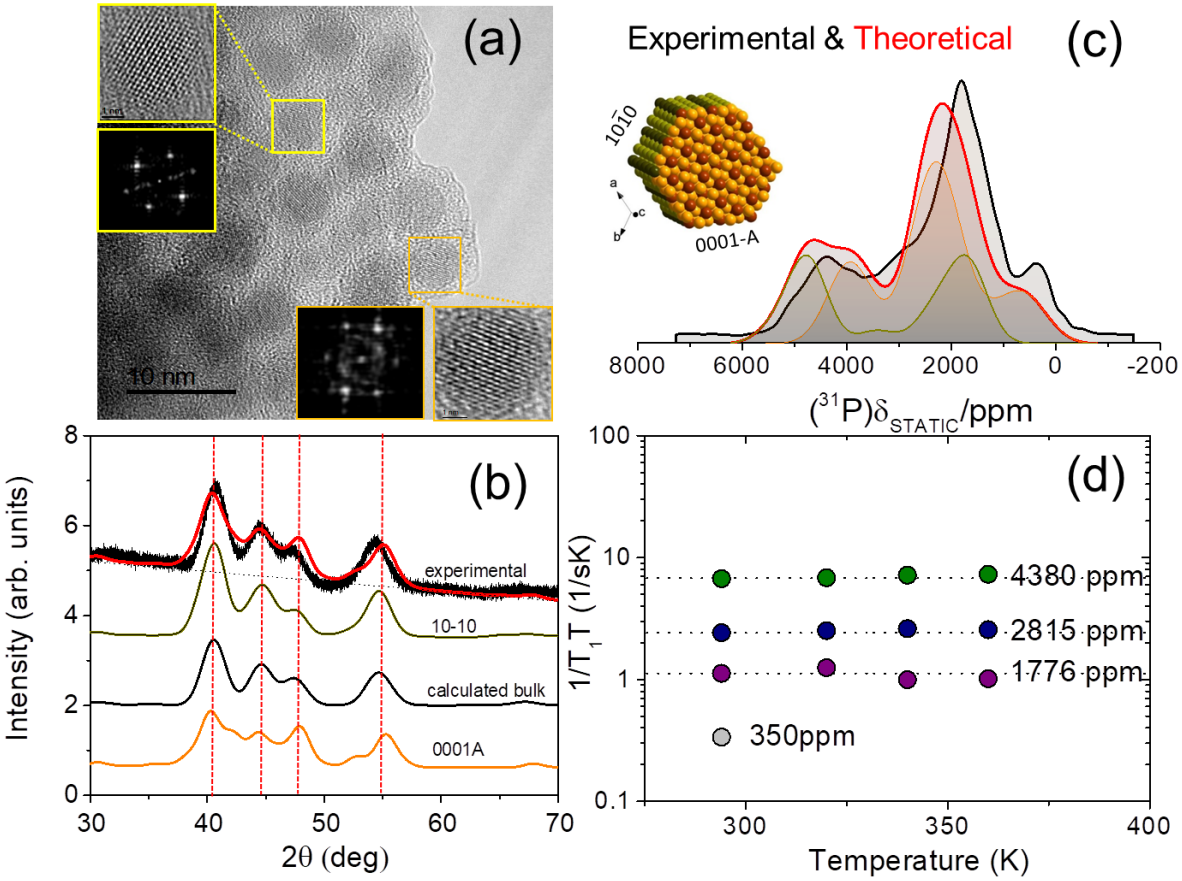

Fig. 5. TEM, XRD and ^{31}P ssNMR analysis of ultrafine Ni_2P nanoparticles with average particle size of 4.3 nm. **a.** TEM image of the nanoparticles exhibiting the hexagonal symmetry. Insets show magnified images of nanoparticles and the relevant EDPs, which match the calculated EDPs of the $10\bar{1}0$ facet (Figure 4e). Further details are provided in Supplementary Information Figure 4. **b.** Experimental (black) and calculated (red) XRD patterns of the

nanoparticles. The orange/green/black traces are calculated XRD simulations of the 0001-A, $10\bar{1}0$, and bulk structures, with Gaussian broadening of the diffraction peaks. The calculated fit (red line) is approximated by the sum of the 0001-A and $10\bar{1}0$ patterns in ratio 1.77:1. **c.** Experimental (black) and calculated (red) ^{31}P ssNMR spectrum of the nanoparticles. The orange/green traces are the surface 0001A/$10\bar{1}0$ contributions in the ratio 1.77:1. The inset is sketch of the expected average facet morphology. **d.** $1/T_1T$ vs temperature for the peaks in the NMR spectrum for the ultrafine nanoparticles.

Figure 6 shows the experimental and calculated TEM and ssNMR results for Ni_2P nanoparticles with average size ~6.5 nm, grown on reduced graphene oxide (r-GO). Details on the synthesis of the r-GO-supported Ni_2P are provided in the Materials and Methods section. Notably, the theoretical NMR spectrum matches the experimental spectrum only in the case where the NMR signal from the $10\bar{1}0$ facet (olive color line) has a greater contribution than the signal from the 0001-A facet. This is a strong indication of the formation of elongated nanoparticles along the 0001 direction with lateral $10\bar{1}0$ facets. In favour of this scenario are the high-resolution TEM (HRTEM) results presented in Figure 6c; the inset with the magnified image region nearly parallel to the (0001) zone axis, exhibits the same crystal structure as the simulated TEM image of the DFT-relaxed $10\bar{1}0$ facet in Figure 6d. Furthermore, experimental and calculated EDPs are in excellent agreement with those in Figure 6a.

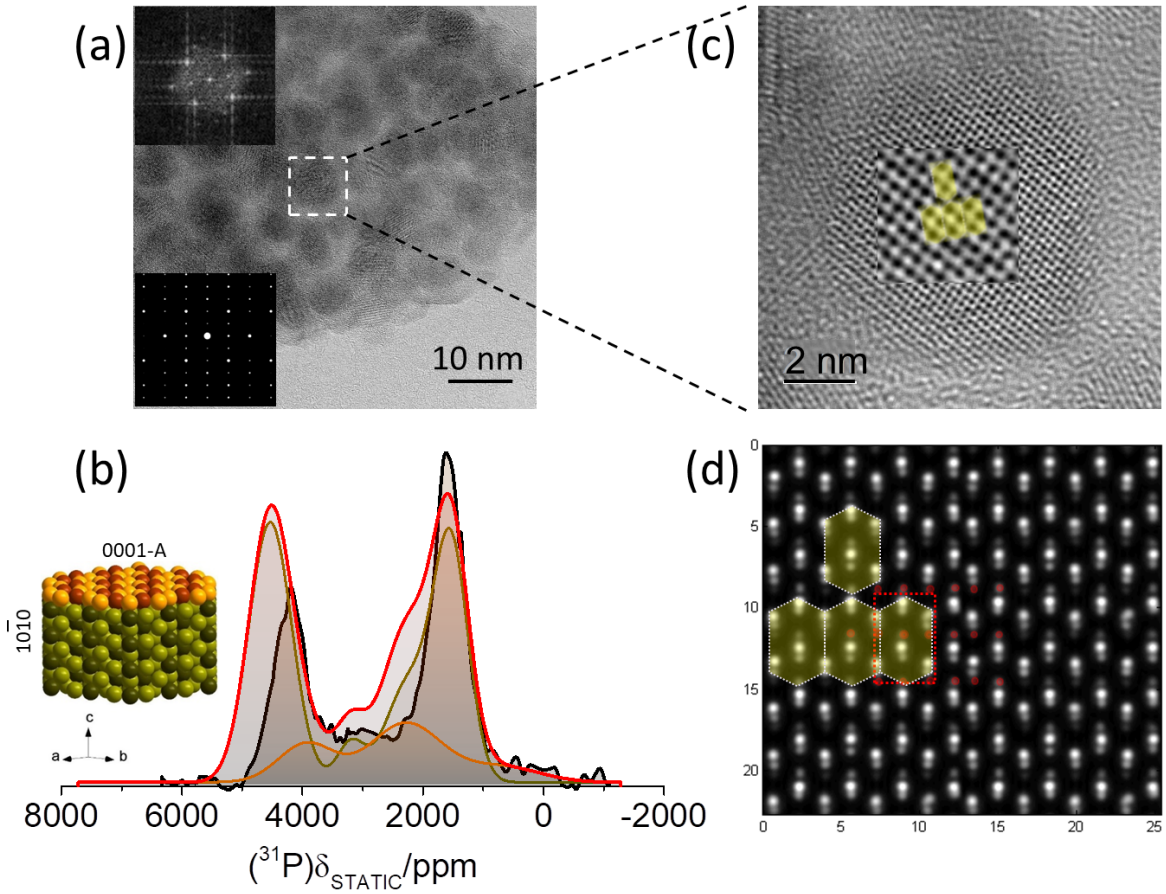

Fig. 6. TEM, and ^{31}P ssNMR analysis of Ni_2P nanoparticles of mean size 6.5 nm grown on reduced graphene oxide. **a.** TEM image of the nanoparticles. The upper inset shows the experimental EDP of the highlighted nanoparticle. The lower inset shows the EDP of the DFT calculated TEM of the $10\bar{1}0$ facet slab. **b.** Experimental (black) and calculated (red) ^{31}P ssNMR spectrum of the nanoparticles. The orange/olive colour traces are the surface 0001-A/$10\bar{1}0$ contributions, respectively. **c.** HRTEM of the highlighted Ni_2P nanoparticle in a. The magnified region showcases the $10\bar{1}0$ facet crystal structure along the (0001) zone axis. **d.** The calculated TEM image of the DFT relaxed $10\bar{1}0$ facet slab. Red color spots are P atoms (not observed experimentally). The red dotted rectangle is the unit cell projected onto the (a,b) plane.

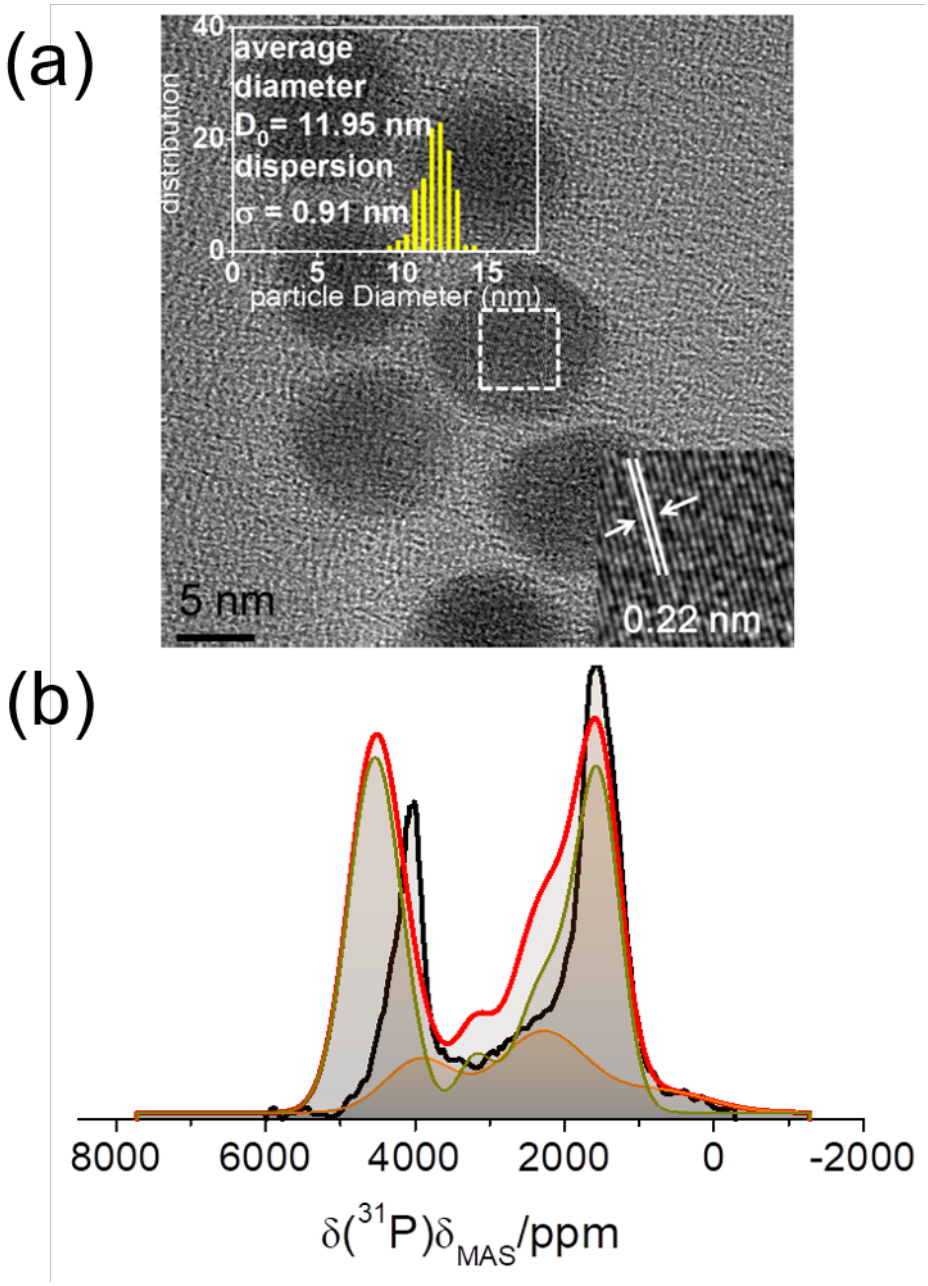

Fig. 7. TEM image and ^{31}P ssNMR spectrum of a Ni_2P nanoparticles sample with average particle size of 12 nm **a.** The TEM image of the nanoparticles. The insert shows the average particle size distribution and the interlayer distance. **b.** Experimental (black) and calculated (red) ^{31}P ssNMR spectrum of the nanoparticles. The orange and olive traces are the estimated contributions of the 0001A and $10\bar{1}0$ terminating structures, respectively. The $10\bar{1}0$ surfaces dominate in the spectrum.

The same situation as shown in Figure 6 for 6.5 nm nanoparticles appears to also be reproduced for the 12 nm Ni_2P nanoparticles, whose spectrum is initially presented in Figure 2 and analyzed in Figure 7. In the high resolution TEM image in the inset of Figure 7a, the

measured distance between the lattice fringes corresponds to 2.21Å, which matches with the 111 plane in Ni_2P[35]. No information about the eventual facets can be revealed from the TEM and the relevant XRD presented in Supplementary Figure 1b. On the contrary the ^{31}P ssNMR spectrum in Figure 7 shows unambiguously that the $10\bar{1}0$ facet dominates, indicating Ni_2P nanoparticles to acquire similar rod-like shapes, as illustrated in Figure 6b.

Discussions

^{31}P DFT-assisted solid-state NMR combined with HRTEM and XRD crystal structure analysis were successfully employed to identify the individual crystal facets of the terminating surfaces of Ni_2P nanoparticles. It is shown that mainly two facets contribute to the experimental results, the 0001-A and the $10\bar{1}0$ surfaces, with the former being the dominant terminating surface of the ultrathin nanoparticles. Notably, as the nanoparticles grow in size, the $10\bar{1}0$ facet appears to prevail over the 0001-A facet, indicating that nanoparticles acquire a nanorod-like shape with lateral $10\bar{1}0$ surfaces along the (0001) zone axis. As the exposure of both the 0001-A and $10\bar{1}0$ facets shifts the Ni electron d-bands towards the Fermi level, the augmented catalytic activity of the Ni_2P nanoparticles is explained in the frame of the d-band model of catalysis[26]. It is noticed that since NMR is a local probe, the method is applicable even for particle sizes of a few nanometers, where most other techniques for structural characterization fail. This makes the method an unprecedented tool in understanding the complex structural and electronic properties of important nanocatalysts.

Materials and Methods

Synthesis of Ni_2P nanoparticles. The microcrystalline (bulk) Ni_2P sample was procured from SIGMA–ALDRICH. Ni_2P and $Ni_{12}P_5$ nanoparticles were synthesized using a slight modification of previously reported liquid phase approach based on solvothermal phosphidation using tri-octylphosphine (TOP), as phosphorous source in oleyl amine enviroment.[36] Specifically, for the case of metal rich $Ni_{12}P_5$ phase, a portion of 0.5 mmol of $Ni(acac)_2$ was dissolved in 20 mL of oleylamine containing 2 mmol of TOP. After complete dissolution of the nickel salt, which takes place at 100 ^oC, the reaction mixture was heated at 280 ^oC and kept at this temperature for 1 h. The synthesis of the phosphorous rich Ni_2P phase took place in an oleyl amine/octadecene mixture at 330 ^oC. Both the temperature increment and oleyl amine replacement enhance the phosphidation process allowing the formation of the pure phosphorous rich phase while lower reaction temperature and oleyl amine enhance the

formation of the metal rich phase. All the reaction steps took place under inert atmosphere. The reaction mixture changed progressively from green to dark green and finally to black indicating the formation of the phosphide nanoparticles. The nanoparticles were precipitated, after cooling at room temperature, by adding ethanol and separated by centrifugation. This precipitation/separation procedure was repeated twice in order to remove the excess of the organic molecules and reaction by-products.

The Ni_2P/r-GO hybrids were synthesized following similar methodology, with sonochemical GO exfoliation before the Ni_2P formation, as described in ref.[37]. The main difference in this case is the replacement of octadecene with tri-octylamine. The tri-octylamine, in contrast with octadecene, functionalize more efficiently, and consequently exfoliate better, the GO flakes, and additionally the competitive adsorption with the primary amine, due to steric effects, on the nickel surface enhance the phosphidation process leading to the formation of the phosphorous-rich Ni_2P phase. In particular, GO were first dispersed in the aliphatic amines (oleyl amine/tri-octylamine) mixture and probe sonicated in order to exfoliate them, following by the drop-wise addition of the $Ni(acac)_2$ solution in a similar aliphatic amines mixture which additional includes the phosphorous source, (TOP). The reaction mixture was then removed from the sonication source and heated up to 300 ^oC for 2 h under a nitrogen blanket. The products separated first by centrifugation and washed twice with a 1/1 ethanol-hexane mixture in order to remove the excess of the organic solvents and reaction by-products, and finally stored in $CHCl_3$.

Solid-state NMR. The ^{31}P MAS experiments were performed with a 4 mm HXY triple-resonance probe, at 14 kHz MAS on a Bruker 400 Avance-III spectrometer operating at a ^{31}P Larmor frequency of 161.976 MHz. Spectral acquisition was done with a double adiabatic spin-echo sequence (DAE) with a 5.0 μs $\pi/2$ excitation pulse length, corresponding to an RF field of 50 kHz, followed by a pair of rotor-synchronized tanh/tan short high-power adiabatic pulses (SHAPs)[38,39] of 71.43 μs length and 5 MHz transmitter frequency sweep. Three subspectra acquired using the variable offset cumulative spectroscopy (VOCS) method were summed[40]. Chemical shifts were referenced to H_3PO_4 85 % wt at 0 ppm.

The ^{31}P static NMR experiments were performed at magnetic field of 9.4 T using a home-built broadband coherent pulsed NMR spectrometer. An Oxford furnace was employed for high temperature measurements. The NMR spectra were obtained using a home-built probe and employing the standard Hahn spin-echo pulse sequence while varying the frequency across the NMR line. The $\pi/2$ pulse length of the rf pulses was set to 3.5 μsec.

XRD. The XRD patterns were acquired with a Siemens D500 powder diffractometer with Cu-Kα radiation (λ = 1.5418 Å). In order to enhance the intensity and resolution of the diffraction maxima, a Bragg–Brentano focusing geometry was used. X-ray patterns were recorded at an angular range (2θ) of 20 – 100° and at a scanning rate 0.5°/min. The Rietveld refinement of obtained powder XRD pattern was carried out using the FULLPROF program software. Refined parameters include: overall scale factor, background (BGP), lattice parameters, atomic positions and orientation. DFT Calculated XRD patterns were acquired using the VESTA software[41].

TEM. Transmission Electron Microscopy studies were carried out with a Jeol 2011 electron microscope and a FEI Tecnai G20, both operating at 200 kV. For this analysis, approximately 2 mg of each sample was dispersed in 20 ml of high purity cyclohexane (Merck, 99.9 %) via sonication (~15 s); then a drop of each suspension was deposited on carbon-coated grids (400 mesh) covered with thin amorphous carbon film (lacey carbon). To avoid contamination, specimens were inserted in the TEM immediately following preparation. Bright field images were collected at several magnifications in order to observe structure and size homogeneity. Calculated HRTEM images were obtained with the help of the MacTempasX software, Total Resolution LLC. The simulated electron diffraction pattern images were obtained with the SingleCrystal software (CrystalMaker Software Ltd.).

DFT calculations. DFT calculations were performed using the QUANTUM ESPRESSO Simulation Package code[42]. The Perdew-Burke-Ernzerhof exchange-correlation functional with the generalized gradient approximation[43] was used. The Projector-Augmented Wave approach (PAW)[44] was used together with plane wave basis sets. In case of bulk Ni_2P, calculations were performed by inserting in the DFT calculations the lattice parameters from the Rietveld analysis. The kinetic energy cutoff of 480 eV was used and the Brillouin zone was sampled by a 12x12x12 Monkhorst-Pack mesh[45]. The z-axis was taken as normal to the surface.

The Ni_2P nanoparticles were modeled with a Ni_2P super-cell comprised of 5 to 11 Ni_2P unit cells (successive Ni_3P_2 and Ni_3P layers), terminated with Ni_3P_2 in case of the 0001-A slab, and Ni_3P in case of the 0001-B slab. The 0001-A-P structure was taken from ref. 15, whereas the $10\bar{1}0$ surface comprised of a 54 atoms super-cell was designed with the VESTA software. All structures were relaxed using the Broyden–Fletcher–Goldfarb–Shanno (BFGS) algorithm [46]. The kinetic energy cut-off was set 480 eV and a 12x12x1 Monkhorst-Pack mesh was used.

NMR Knight shift calculations were performed on bulk Ni_2P, and the 4 different Ni_2P slabs by using the full-potential linearized augmented plane-wave method, as implemented in the Wien2k DFT software package[32]. The *k*-mesh convergence was checked up to 100,000 points

for the bulk materials and up to 5,000 points for the slabs. Other computational parameters, such atomic sphere radii as well as potentials and wave functions inside the atomic spheres, were as set by Wien2k defaults. The plane wave basis set size was determined by setting $RK_{max}=8$, whereas for presented results we have used the LDA approximation[43]. All structures, including the bulk material were structurally relaxed. In case of the bulk material the initial lattice parameters were taken from the Rietveld analysis of the XRD pattern.

Data availability: The authors declare that the data supporting the findings of this study are available within the article and its Supplementary Information file. Extra data are available from the corresponding authors upon reasonable request.

Acknowledgments: W.P., J.P.C. and A.J.P. were supported by the Swedish Research Council (project no. 2016-03441) and the Swedish National Infrastructure for Computing (SNIC) through the center for parallel computing (PDC), project number 2019-3-500. N.P., V.T., M.K., M.F. and G.P. acknowledge support by the project MIS 5002567, implemented under the "Action for the Strategic Development on the Research and Technological Sector", funded by the NSRF 2014-2020 and co-financed by the European Union and Greece. Part of the DFT work was performed using computational resources of the Research Computing Department at Khalifa University. X.L, K.P, G.P., and Y.A. would like to acknowledge the support of Khalifa University of Science and Technology Award No. RC2-2018-024.

Authors Contribution: A.J.P., W.P., Y.A., and G.P. conceived and designed the experiments, performed theoretical analysis, and did the majority of paper writing (with additional contributions from all coauthors). MAS NMR experiments and data analysis were performed by W.P., J.P.C., A.J.P., and V.K. Frequency sweep static NMR and relaxation studies were performed by W.P., N.P., M.K., and M.F. DFT calculations and comparison with experiments were performed by W.P., Y.A., J.P.C., and G.P. Ni_2P nanoparticle preparation and characterization was performed by X.L., K.P., and V.T. HRTEM experiments and simulations were performed by J.B.L., S.L., C.Y.K., H.J.K., and M.K.

Competing Interests: The authors declare no competing interests.

References and Notes:

1. Maxwell, I. E. Driving forces for studies in catalysis. *Stud. Surf. Sci. Catal.* **101**, 1-9 (1996).
2. Greeley, J. Electronic Structure and Catalysis on Metal Surfaces. *Annu. Rev. Phys. Chem.* **53**, 319–348 (2002).

3. Nørskov, J.K. T. Density Functional Theory in Surface Chemistry. PNAS **108**, 937–943 (2011).
4. Jun, Y. W., Choi, J. S. & Cheon, J. Shape control of semiconductor and metal oxide nanocrystals through nonhydrolytic colloidal routes. *Angew. Chem. Int.Ed*. 45, 3414–3439 (2006).
5. Liu, D., Xu, X., Du, Y. et al. Three-dimensional controlled growth of monodisperse sub-50 nm heterogeneous nanocrystals. *Nat. Commun.* **7,** 10254 (2016).
6. Wang, Z. *et al.* Morphology-tuned wurtzite-type ZnS nanobelts. *Nature Mater* **4,** 922–927 (2005).
7. Popczun, E. J., et al. Nanostructured Nickel Phosphide as an Electrocatalyst for the Hydrogen Evolution Reaction. *J. Am. Chem. Soc.* **135**, 9267-9270 (2013).
8. Stern, L.-A., Feng, L., Song, F., Hu, X. Ni_2P as a Janus catalyst for water splitting: the oxygen evolution of Ni_2P nanoparticles. *Energy Environ. Sci.* **8**, 2347-2351 (2015).
9. Liu, P., Rodriguez, J. A., Takahashi, Y. et al. Water–Gas-Shift Reaction on a Ni_2P (001) Catalyst: Formation of Oxy-Phosphides and Highly Active Reaction Sites. *J. Catal.* **262**, 294– 303 (2009).
10. Oyama, S. T., Gott, T., Zhao, H. & Lee, Y. K. Transition metal phosphide hydroprocessing catalysts: a review. *Catal. Today.* **143**, 94–107 (2009).
11. Li, Q.; Hu, X. First-principles study of Ni_2P (0001) surfaces. *Phys. Rev. B: Condens. Matter Mater. Phys.* **74**, 035414 (2006).
12. Kanama, D., Oyama, S., Otani, S. et al. Photoemission and LEED characterization of Ni_2P (0001). *Surf. Sci.* **552**, 8–16 (2002).
13. Moula, M.G. et al. The first atomic-scale observation of a Ni_2P(0001) single crystal surface. *Chem. Lett.* **35**, 90– 91 (2006).
14. Jung, C. S. et al. Nickel Phosphide Polymorphs with an Active (001) Surface as Excellent Catalysts for Water Splitting. *CrystEngComm* 21 (7), 1143– 1149 (2019).
15. He, J., Morales-Garcia, A., Bludsky, O. et al. The Surfaces Stability and Equilibrium Crystal Morphology of Ni_2P Nanoparticles and Nanowires from ab initio Atomistic Thermodynamic Approach. *CrystEngComm* **18**, 3808-3818 (2016).
16. Papawassiliou, W., Jaworski, A., Pell, A. J. *et al.* Resolving Dirac electrons with broadband high-resolution NMR. *Nat Commun* **11,** 1285 (2020).
17. Li, Y., Wu, X., Jiang, N. *et al.* Distinguishing faceted oxide nanocrystals with ^{17}O solid-state NMR spectroscopy. *Nat Commun* **8,** 581 (2017).
18. Hanrahan, M. P. et al. Probing the Surface Structure of Semiconductor Nanoparticles by DNP SENS with Dielectric Support Materials. *J. Am. Chem. Soc*. **141**, 15532−15546 (2019).
19. Piveteau, L. et al. Structure of Colloidal Quantum Dots from Dynamic Nuclear Polarization Surface Enhanced NMR Spectroscopy. *J. Am. Chem. Soc.* **137**, 13964−13971 (2015).
20. Laskowski, R. & Blaha, P. NMR Shielding in Metals Using the Augmented Plane Wave Method. *J. Phys. Chem. C* **119,** 19390−19396 (2015).
21. Knight, W. D. Nuclear Magnetic Resonance Shift in Metals. *Physical Review* 1949, 76, 1259-1260.
22. Slichter, C. P. Principles of Magnetic Resonance. *Springer, Berlin*, (1990).
23. Hope, M. A. *et al.* The role of ionic liquid breakdown in the electrochemical metallization of VO_2: An NMR study of gating mechanisms and VO_2 reduction. *J. Am. Chem. Soc.* **140**, 16685–16696 (2018).
24. Marbella, L. E. et al. Correlating Carrier Density and Emergent Plasmonic Features in $Cu_{2-x}Se$ Nanoparticles. *Nano Lett.* **17**, 2414– 2419 (2017)
25. Korringa, J. Nuclear magnetic relaxation and resonnance line shift in metals. *Physica* **16**, 601–610 (1950).

26. Hammer, B., Norskov, J. K. Theoretical Surface Science and Catalysis—Calculations and Concepts. *Advances in Catalysis* **45**, 71-129 (2000).
27. Bekaert, E., et al. Direct Correlation Between the ^{31}P MAS NMR Response and the Electronic Structure of Some Transition Metal Phosphides. *J. Phys. Chem. C* **112**, 20481–20490 (2008).
28. Rundqvist, S. X-Ray Investigations of Mn_3P, Mn_2P and Ni_2P. *Acta Chemica Scandinavica* **16**, 992–998 (1962).
29. Rundqvist, S. and Larsson, E., The Crystal Structure of $Ni_{12}P_5$, *Acta Chem. Scand.,* **13**, 551-560 (1959).
30. Mayo, M., Griffith, K. J., Pickard, C. J. & Morris, A. J. Ab initio study of phosphorus anodes for lithium- and sodium-ion batteries. *Chem. Mater*. **28**, 2011–2021 (2016).
31. Cadars, S. et al. *Phys. Rev. Lett.* **103**, 136802 (2009).
32. Blaha, P. et al., An augmented plane wave plus local orbitals program for calculating crystal properties. Vienna University of Technology, Austria, ISBN 3-9501031-1-2 (2001).
33. Hansen, M. H., et al. Widely available active sites on Ni_2P for electrochemical hydrogen evolution. *Phys. Chem. Chem. Phys.* **17**, 10823 (2015).
34. Clément, R. J., Kitchaev, D., Lee, J. & Gerbrand, C. Short-range order and unusual modes of nickel redox in a fluorine-substituted disordered rocksalt oxide lithium-ion cathode. *Chem. Mater.* **30**, 6945–6956 (2018).
35. Hernandez, A. et al. Dynamical LEED analysis of Ni_2 P (0 0 0 1)-1 × 1: Evidence for P-covered surface structure. *Chem. Phys. Lett.* **513**, *513*, 48– 52 (2011).
36. Zafiropoulou, I., et al. Chemical Synthesis and Self-Assembly of Hollow Ni/Ni_2P Hybrid Nanospheres. *J. Phys. Chem. C* **114**, 7582–7585 (2010).
37. Tzitzios, V., et al., Ultra-fine Ni_2P nanoparticles decorated r-GO: Novel Phosphidation approach and Dibenzothiophene Hydrodesulfurization. ChemRxiv. Preprint. https://doi.org/10.26434/chemrxiv.12706235.v1 (2020).
38. Pell, A. J. et al. Paramagnetic NMR in solution and the solid state. *Prog. Nucl. Magn. Reson. Spectrosc.* **111,** 1-271 (2019).
39. Kervern, G. et al. Fast adiabatic pulses for solid-state NMR of paramagnetic systems. Chem Phys Lett. **435**, 157–162 (2007).
40. A. Medek, V. Frydman, L. Frydman, Central Transition NMR in the Presence of Large Q uadrupole Couplings: Cobalt59 NMR of Cobaltophthalocyanines, *J. Phys. Chem. A*. **103** 4830-4835 (1999).
41. Momma, K. & Izumi, F. VESTA: A three-dimensional visualization system for electronic and structural analysis. *J. Appl. Cryst.* **41**, 653–658 (2008).
42. Ceresoli, D. et al., Quantum Espresso: a modular and open-source software project for quantum simulation of materials. *J. Phys.:Condens.Matt.* **21**, 395502 (2009).
43. Perdew, J. P., Burke, K., Ernzerhof, M. Generalized Gradient Approximation Made Simple. *Phys. Rev. Lett.* **77**, 3865-3868 (1996).
44. Blochl, P., E. Projector augmented-wave method. *Phys. Rev. B* **50**, 17953–17979 (1994).
45. Monkhorst, H. J.; Pack, J. D. Special points for Brillouin-zone integrations. Phys. Rev. B 1976, 13, 5188–5192.
46. Dennis J. E.; Schnabel R. B. Numerical Methods for Unconstrained Optimization and Nonlinear Equations. Prentice-Hall, Englewood Cliffs, NJ (1983).